

# A scalable and real-time neural decoder for topological quantum codes

Andrew W. Senior<sup>1†\*</sup>, Thomas Edlich<sup>1†</sup>, Francisco J.H. Heras<sup>1†</sup>,  
Lei M. Zhang<sup>1</sup>, Oscar Higgott<sup>2</sup>, James S. Spencer<sup>1</sup>, Taylor Applebaum<sup>1</sup>,  
Sam Blackwell<sup>1</sup>, Justin Ledford<sup>2</sup>, Akvilė Žemgulytė<sup>1</sup>, Augustin Žídek<sup>1</sup>,  
Noah Shutty<sup>2</sup>, Andrew Cowie<sup>1</sup>, Yin Li<sup>1</sup>, George Holland<sup>1</sup>, Peter Brooks<sup>2</sup>,  
Charlie Beattie<sup>1</sup>, Michael Newman<sup>2</sup>, Alex Davies<sup>1</sup>, Cody Jones<sup>2</sup>,  
Sergio Boixo<sup>2</sup>, Hartmut Neven<sup>2</sup>, Pushmeet Kohli<sup>1</sup>, Johannes Bausch<sup>1†\*</sup>

<sup>1</sup>Google DeepMind & <sup>2</sup>Google Quantum AI

Fault-tolerant quantum computing will require error rates far below those achievable with physical qubits. Quantum error correction (QEC) bridges this gap, but depends on decoders being simultaneously fast, accurate, and scalable. This combination of requirements has not yet been met by a machine-learning decoder, nor by any decoder for promising resource-efficient codes such as the colour code. Here we introduce AlphaQubit 2, a neural-network decoder that achieves near-optimal logical error rates for both surface and colour codes at large scales under realistic noise. For the colour code, it is orders of magnitude faster than other high-accuracy decoders. For the surface code, we demonstrate real-time decoding faster than  $1\mu\text{s}$  per cycle up to distance 11 on current commercial accelerators with better accuracy than leading real-time decoders. These results support the practical application of a wider class of promising QEC codes, and establish a credible path towards high-accuracy, real-time neural decoding at the scales required for fault-tolerant quantum computation.

---

\*Corresponding authors

†Equal contribution

# 1. Main

Quantum computation promises significant advantages over classical computers, with potential applications in fields such as physics simulation [1], cryptography [2], and optimization [3]. Realising this potential, however, depends on reliably executing complex algorithms on quantum hardware that is intrinsically noisy and error-prone.

The established route to reliable quantum computation is quantum error correction (QEC), which protects information by encoding a single logical qubit across multiple physical qubits [4]. Below a critical physical error rate threshold, increasing this redundancy exponentially suppresses the logical error rate. Nevertheless, the magnitude of the challenge is substantial: fault-tolerant computations, such as the factorization of a 2,048-bit number, will require logical error rates below  $10^{-10}$  per logical operation [5, 6], seven orders of magnitude below today's typical superconducting physical error rates [7].

Experimental progress towards fault-tolerance is accelerating, with recent demonstrations across multiple hardware platforms confirming the foundational principle of QEC. These efforts have primarily focused on two leading planar codes: the surface code, known to have the highest error threshold of all planar codes [8]; and colour codes, attractive for their more efficient logical operations [9] and lower error correction overhead when implementing a universal gate set [10, 11]. Recent experiments have demonstrated the suppression of logical errors with increasing code size in superconducting qubits (both in surface [7, 12] and colour [13] codes) and neutral atoms [14]. The practical viability of any code, however, depends critically on the classical processing component of error correction: the decoder.

QEC codes, including the surface and colour codes, produce a sequence of parity checks (the error syndrome), which the decoder must interpret in real time to decide whether the logical qubit needs correcting. To be viable, a decoder must simultaneously satisfy two stringent requirements. The first requirement is high decoding accuracy, even during logical operations [13, 15]. For a given physical error rate, achieving higher accuracy requires scaling to larger code distances involving more physical qubits. The second requirement is a decoding speed faster than the hardware's clock cycle (e.g.  $\sim 1 \mu\text{s}$  for superconducting devices [7],  $\sim 1 \text{ ms}$  for neutral atoms [16]) lest an exponential backlog render error correction infeasible [17]. While machine learning (ML) has emerged as a promising paradigm [14, 15, 18–23], no ML-based decoder has yet met these combined demands, particularly for the promising but challenging-to-decode colour code [24].

Here we introduce AlphaQubit 2 (AQ2), a neural network decoder that makes substantial progress towards fulfilling both accuracy and speed requirements. AQ2 achieves near-optimal

accuracy at large scales, reaching logical error rates below  $10^{-10}$  per cycle for the surface and colour codes. For the colour code, it is orders of magnitude faster than available implementations of highly accurate decoders. Furthermore, we show that a real-time variant of AQ2 can decode a surface-code logical qubit formed of up to 241 physical qubits in under 1  $\mu$ s per cycle on commercial hardware—with minimal loss in accuracy. This combination of large-scale accuracy and real-time throughput up to intermediate code distances allows us to outline a viable path to real-time decoding of superconducting qubits at sufficient speed and scale to enable fault-tolerant quantum computation.

## 2. Decoding surface and colour codes

The surface code has been the primary focus of experimental QEC on superconducting hardware (Fig. 1a,d). It encodes a logical qubit on a grid of  $d \times d$  data qubits, and uses an interspersed set of  $d^2 - 1$  measure qubits to periodically execute X and Z stabilizer parity checks on adjacent data qubits. A detection event occurs when stabilizer checks in two consecutive cycles of measurements disagree (Fig. 1a). The logical state of the surface code is determined by a pair of observables,  $X_L$  and  $Z_L$ , which anti-commute with each other and commute with all stabilizers. The side length,  $d$ , of the grid is the same as the code distance, i.e. the minimum number of physical qubit errors required for an undetectable logical error.

Decoding the surface code is a mature field, dominated by the Minimum Weight Perfect Matching algorithm (MWPM) and its variants [25, 26] (e.g. PyMatching [27, 28]). While highly efficient, MWPM provides only an approximate solution. Recently, augmented variants of MWPM have demonstrated higher accuracy by ensembling matching solutions (Libra [29] and Harmony [30]) or by generalizing MWPM to hypergraphs (Minimum-Weight Parity Factor [31]). Tesseract [32] can achieve near-optimal accuracy by using A\*-search to find the most likely error source, at considerable computational cost.

This highlights a persistent trade-off between decoding speed and accuracy [31, 33].

Colour codes are an alternative that may require fewer physical qubits and facilitate implementation of logical operations [9–11]. In this paper, we focus on the Bell-flagged triangular colour code [34, 35], where data qubits are arranged on the vertices of a honeycomb lattice (Fig. 1d). Each hexagonal cell defines an X and a Z stabilizer. A full error-correction cycle consists of reading all X stabilizers, followed by all Z stabilizers. The readout is mediated by two measure qubits within each hexagonal cell, one of them acting as a “flag” to signal potential errors during readout (see Methods).

Developing effective decoders for colour codes has been a significant challenge, which has likely played a role in hampering their experimental adoption [13]. Existing decoders again illustrate a trade-off between speed and accuracy. While Tesseract can be applied to colour codes, it is very computationally intensive. In contrast, Chromobius [24] has been specifically designed to work with the colour code and is fast but has considerably lower accuracy. More recent approaches fall between these two extremes [36, 37]. To date, the lack of a decoder that is simultaneously fast, accurate, and scalable has been a significant barrier to leveraging the colour code’s potential advantages.

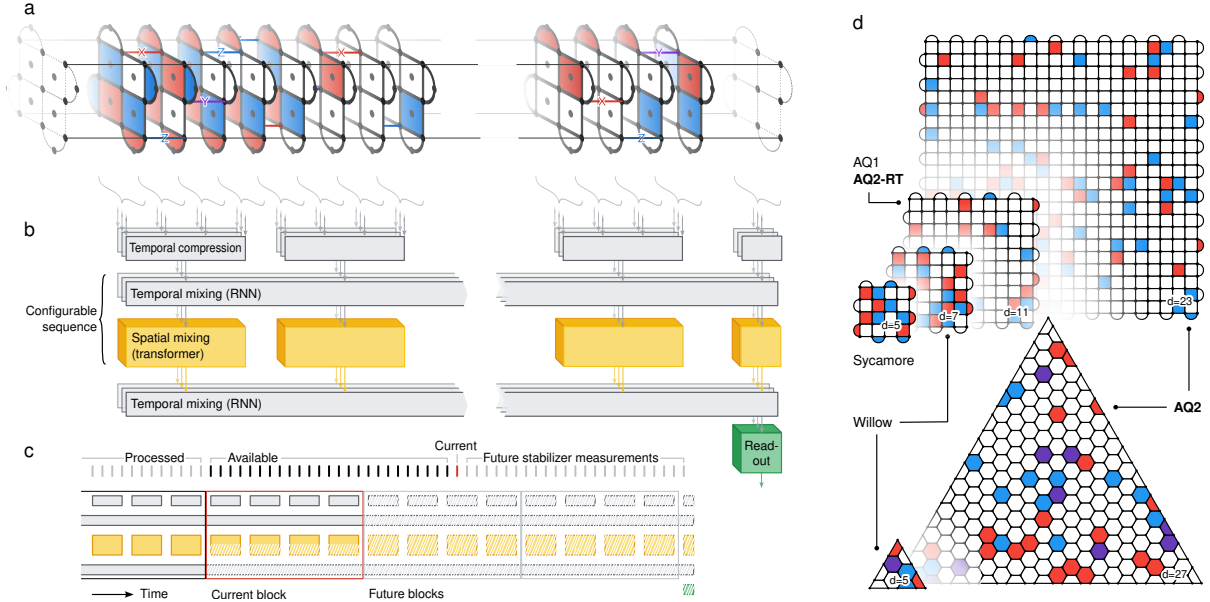


**Figure 1: Decoding memory experiments with AlphaQubit 2 (AQ2). a,** In a surface code memory experiment, a logical qubit is initialized; repeated stabilizer checks are performed; and then the logical qubit state is measured. During the experiment all qubits and operations are subject to errors (here symbolically shown as bit (X), phase (Z), and combined bit and phase flips (Y) acting on individual data qubits between time steps). These errors affect the stabilizer parity checks (X check failure in red, Z check failure in blue). **b,** Overview of the AQ2 architecture. Information flows from top to bottom and left-to-right. Consecutive checks for each stabilizer are temporally compressed in groups, then processed by alternating temporal and spatial mixing layers. The output from the last time step is fed to a readout network which makes a prediction of the logical error. **c,** Spatial and temporal mixing updates can be done in a streaming fashion: different temporal windows can be computed as stabilizer measurements are available, without waiting for the experiment to end. **d,** Logical qubit patches for the surface and colour codes (distance 23 and 27, resp.) as decoded by AQ2. Superimposed are the largest surface code sizes previously implemented on Sycamore [12] (distance 5); Willow [7] (distance 7) and decoded by AlphaQubit 1 [18] (distance 11, also decoded in real-time by AQ2-RT); and the distance-5 colour code implemented on Willow [13].

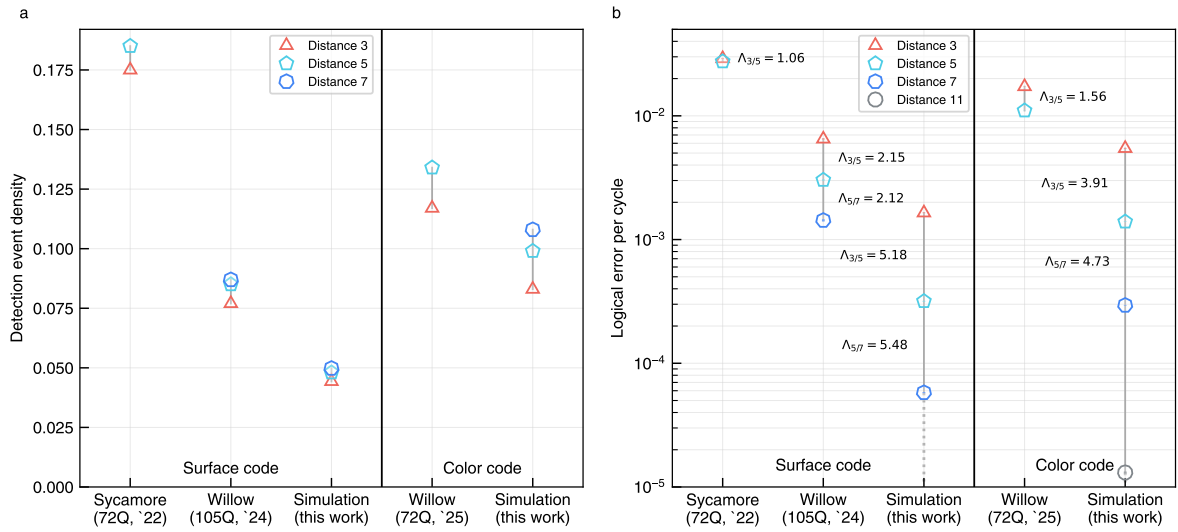


**Figure 2: Progress in superconducting hardware.** **a**, Detection event fraction for surface and colour codes of different distances implemented in two generations of superconducting quantum computing (Sycamore [38] and Willow [7, 13]), compared to the simulated circuit depolarizing noise model (SI1000 [39] at  $p = 0.15\%$ ) chosen for the experiments in this paper, anticipating future hardware improvements. **b**, The corresponding progress in logical error rate for surface and colour codes, when decoded using AlphaQubit 1 [7, 13, 18] (Sycamore and Willow) and AlphaQubit 2 (this work).

### 3. High accuracy decoding

#### 3.1. Neural network decoding

Neural networks are a promising approach for QEC decoding. Diverse strategies, from generative [21, 22] to discriminative [18] models, have been successfully applied to decoding memory experiments in surface, colour and qLDPC codes [13, 20], as well as logical gate operations [13, 15, 19]. While these studies establish the potential of machine learning, they have not yet delivered a decoder that simultaneously achieves the high accuracy and speed required for fault-tolerant quantum computation.

Achieving the logical error rates of  $10^{-10}$  or lower per cycle required for practical fault tolerant quantum algorithms [5, 6, 40] necessitates scaling QEC codes to distances beyond the reach of near-term hardware. Rigorous assessment of decoder performance at these scales therefore depends on large-scale simulation. We generate training, evaluation and test data using Stim [41], employing the SI1000 circuit-level depolarizing noise model which reflects the error characteristics expected of future superconducting hardware [39]. We choose a physical noise level (0.15%) corresponding to an anticipated improvement in hardware performance comparable to the progression from Sycamore to Willow quantum processors. In the surface code, this leads to a detection event density of  $\sim 5\%$  (Fig. 2a) and an error suppression factor of  $\gtrsim 5$  (Fig. 2b).

#### 3.2. A scalable spatiotemporal architecture

AQ2 processes the error syndrome of a logical qubit in a streaming fashion and predicts the logical observable. We designed its architecture (Fig. 1b) to be applicable in principle to experiments of arbitrary code distance and duration, and to leverage accelerator parallel processing both during training and evaluation.

The network is composed of interleaved temporal and spatial layers which compute internal representations for each stabilizer at each error correction cycle. Recurrent neural-network layers implement temporal updates by propagating information forward in time for each stabilizer independently (but sharing parameters), integrating new measurement data with the stabilizer's previous state. Spatial updates are performed by attention-based transformer layers that allow stabilizer representations to exchange information with each other across the entire code patch at a single instant in time. After the final cycle, a readout network aggregates the final state vectors from all stabilizers to predict the probability of a logical error.

To achieve higher speeds both during training and evaluation, instead of performing a temporal update at each measurement cycle, we combine groups of (typically 6) consecutive

measurement cycles, using a learnt temporal compression which results in no loss in accuracy. Processing can be carried out on a block of such groups, in which the computation for all the groups can be carried out in parallel for each spatial transformer layer. Since the architecture propagates information causally, with only the recurrent state vectors carrying information about the syndrome history forward, the computations can be performed in a streaming fashion across blocks, while new stabilizer measurements are received from the quantum computer (Fig 1c).

We train AQ2 following a novel training regime designed for scalability and accuracy; using gradient descent on many millions of examples generated by Stim [41] across a wide range of code distances, error rates, and experiment durations. To enable robust and shorter training, we employ a curriculum learning strategy, where the model is first trained predominantly on easier examples (smaller code distances, short experiments) before progressing to more challenging examples (larger code distances). For the highest code distances, we further fine-tune the model exclusively on examples for a single code distance and ensemble two variants of the model (three for the colour code at distance 27). Furthermore, we introduce two key techniques to stabilize and accelerate learning: a novel auxiliary loss that tasks the network with predicting an idealized, noise-free readout of the logical observable, and a random input dropout method. Details of the network architecture and training process are described in Methods.

### 3.3. Decoding at scale

AQ2 achieves near-optimal accuracy on the surface code up to code distance 23. On simulated 120-cycle memory experiments with 0.15% circuit-level noise, it achieves a logical error per cycle of  $7.3 \times 10^{-11}$  (Fig. 3a). This performance is close to that of the near-optimal, but slower, Libra decoder and substantially outperforms both correlated and uncorrelated PyMatching decoders [27, 28].

Furthermore, AQ2 achieves high-fidelity decoding of the Bell-flagged colour code at large scale (Fig. 3b). There is no fast, high-accuracy decoder for this code. We compare AQ2 performance to the near-optimal Tesseract [32] decoder at small distances ( $d \leq 7$ ). Beyond this distance Tesseract is too slow to evaluate so we extrapolate linearly from distance 5 and 7 to estimate an ideal decoding accuracy. Our results show that AQ2 tracks this idealized performance closely up to distance 23. At distance 27, an ensemble of 3 models reaches a logical error per cycle of  $8.0 \times 10^{-11}$ , but does not match the idealized trend in this regime where training AQ2 is more difficult and expensive (see Methods).

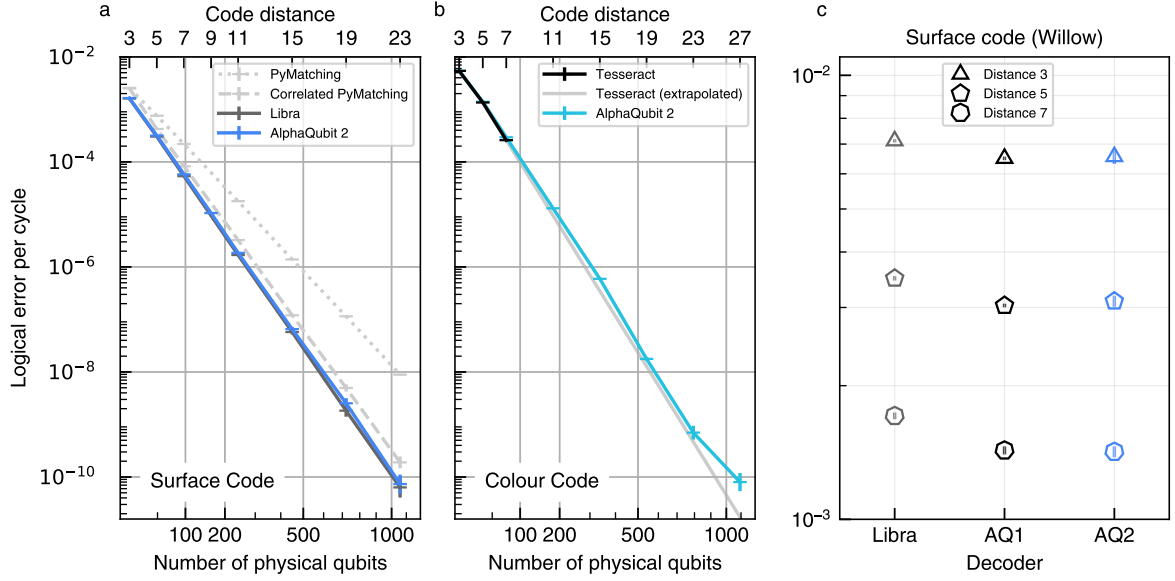


**Figure 3: AlphaQubit 2 (AQ2) accuracy on simulated and experimental data. a, b.** Accuracy at scale: Logical error per cycle against number of physical qubits / code distance for the surface code (a) comparing AQ2 with the Libra decoder and PyMatching and for the colour code (b), comparing AQ2 with extrapolated Tesseract error rates. Measured on up to  $2.5 \times 10^{10}$  shots of 120 cycles from the SI1000 noise model (details in Methods). **c,** Experimental data: logical error per cycle at code distances 3, 5 and 7 for AQ2 on the Willow experimental data [7] compared to the most accurate decoders from the original paper (AlphaQubit 1 & Libra). Error bars are 95% confidence intervals in all figures.

### 3.4. Decoding the Willow experiment

To validate our decoder with data from a physical quantum processor, we applied AQ2 to experimental data from the 105-qubit Willow chip [7], which implements surface codes of distance 3, 5, and 7. We find that our new decoder achieves a logical error rate comparable to that of our previous slower architecture, AlphaQubit (AQ1 [18]), and better than Libra on the same experimental dataset (Fig. 3c). This result was obtained using the three-stage training protocol detailed in our previous work [7]: pretraining on generic simulated noise (SI1000); fine-tuning on simulated samples from a Detector Error Model (DEM) fitted to experimental data; and further fine-tuning on a subset of the experimental samples from the Willow hardware itself.

## 4. Real-time decoding

A primary requirement for practical QEC is real-time decoding, where measurement data must be processed faster than it is generated to avoid incurring an exponential backlog [17]. For superconducting hardware this imposes a demanding average throughput rate of around 1  $\mu$ s per cycle.

AQ2 as described above, in both the surface and the colour code, is more accurate than any faster decoder we compared it against, *i.e.* it sits on the Pareto front of the accuracy-throughput trade-off (Fig. 4a,b). For code distances up to 23, AQ2 has a cycle time below 100  $\mu$ s: fast enough to decode neutral atom or trapped ion circuits (around 1 ms [16, 42]), but too slow to decode superconducting circuits in real time.

To enable decoding on superconducting qubits, we have developed a real-time variant of AQ2 (AQ2-RT). It is a compact version of AQ2 with fewer layers, smaller representations and faster recurrence (see Methods). AQ2-RT achieves this stringent real-time throughput for the surface code up to distance 11 (Fig. 4a,d), using commercially-available machine learning accelerators (Trillium TPUs [43]), without the need for custom hardware such as ASICs or FPGAs.

The throughput improvements of AQ2-RT are substantial (Fig. 4). While the full AQ2 is already 9.6 times faster at distance 11 than AQ1, the real-time variant provides a further 6 times speed-up (Fig. 4a,d).

Both AQ2 and AQ2-RT are streaming decoders whose computational costs do not vary with the errors observed, and whose throughputs can be maintained for longer experiments without any increase in latency, which remains below 500  $\mu$ s (see Methods).

The speed increase of AQ2-RT entails a modest trade-off in accuracy. In the surface code, the real-time decoder's logical error rate is slightly higher than that of the full-accuracy model (Fig. 4a,c), particularly at distance 11 ( $3.73 \times 10^{-6}$  vs  $1.89 \times 10^{-6}$ ). At that code distance, the real-time model remains more accurate than other decoders which can achieve this throughput (a real-time matching decoder [7] and PyMatching for lower code distances).

The accuracy drop of the real-time model is also small on experimental data. To assess this we trained AQ2-RT on the Willow data, with the same pretraining and fine-tuning protocol used above (Fig. 4c). AQ2-RT accuracy is close to that of the full AQ2, and is more accurate than both the original real-time decoder used on this dataset (Willow RT; Fig. 4c) and the Libra decoder. (See Methods for details of the models and timing.)

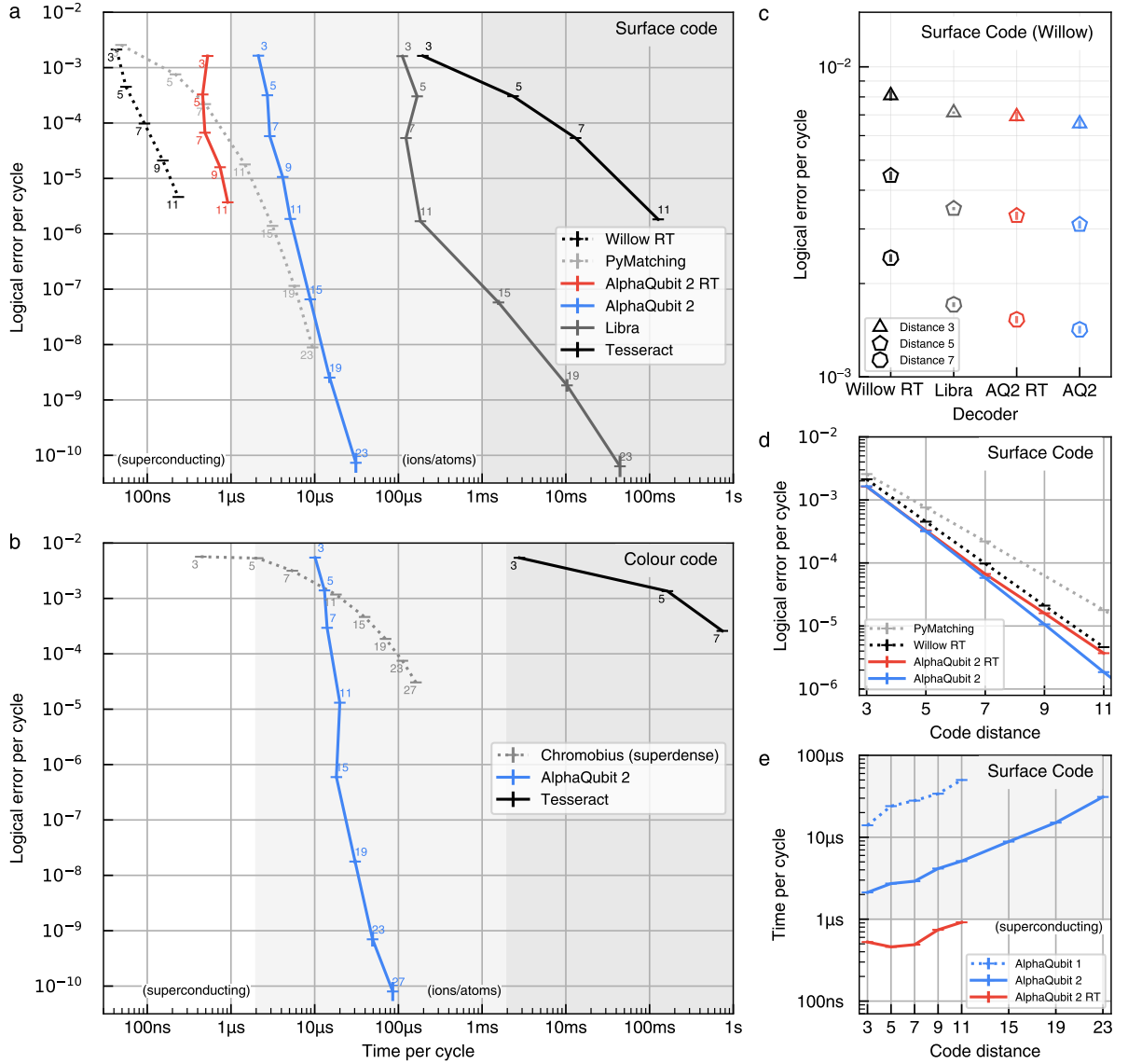


**Figure 4: Accurate, high-throughput decoding of surface and colour codes with AlphaQubit 2 (AQ2).** **a**, Logical error per cycle against throughput (average time per cycle) when decoding the surface code using the real-time (red line) and full (blue line) configurations of AQ2, and other decoders (grey lines) on SI1000 data (0.15% noise) for a range of code distances. Shaded to highlight the 1  $\mu$ s and 1 ms target speeds for superconducting or other hardware substrates with the surface code. Decoders are timed on different hardware (See Methods) **b**, Logical error per cycle against throughput for AQ2 and other decoders (grey lines) on the colour code. Shading above 2  $\mu$ s (2 ms) shows target speeds for superconducting or other hardware substrates with the colour code (Methods). We also show throughput and accuracy for the Chromobius decoder with the superdense colour code using the same noise model. **c**, Logical error per cycle at distance 3, 5 and 7 for AQ2 real-time on the Willow experimental data [7] compared to the real-time matching-based decoder and full AQ2 and decoders from the original paper (AQ1, & Libra). **d**, Logical error per cycle against code distance on SI1000 data (0.15% noise) for the real-time and full AQ2 compared to Tesseract, PyMatching and correlated PyMatching. **e**, Throughput vs code distance for three versions of AlphaQubit. AQ2 is timed on Trillium TPU, AQ1 was timed on the earlier TPU v5e.

## 5. Robustness

A critical requirement for any practical decoder is temporal stability: it must perform reliably over millions of QEC cycles, far longer than is feasible for training. AQ2’s time-invariant, recurrent architecture is explicitly designed for this scenario, enabling it to operate in a streaming fashion with a fixed computational cost per cycle and constant memory requirement. To test this generalization capability, we took a model trained on experiments of maximum length 168 cycles and evaluated it on experiments up to one million cycles. AQ2 maintains a stable logical error per cycle, albeit with a small degradation in performance at distances 19 and 23 (Fig. 5a).

AQ2 is also robust to changes in sample noise strength, without retraining or requiring the noise level as an explicit input. For instance, the decoders for both colour and surface codes perform well across at least a sixteen-fold variation in circuit noise strength, including values above and below the range of circuit noise used for training (See Fig. 5b for distance 11).

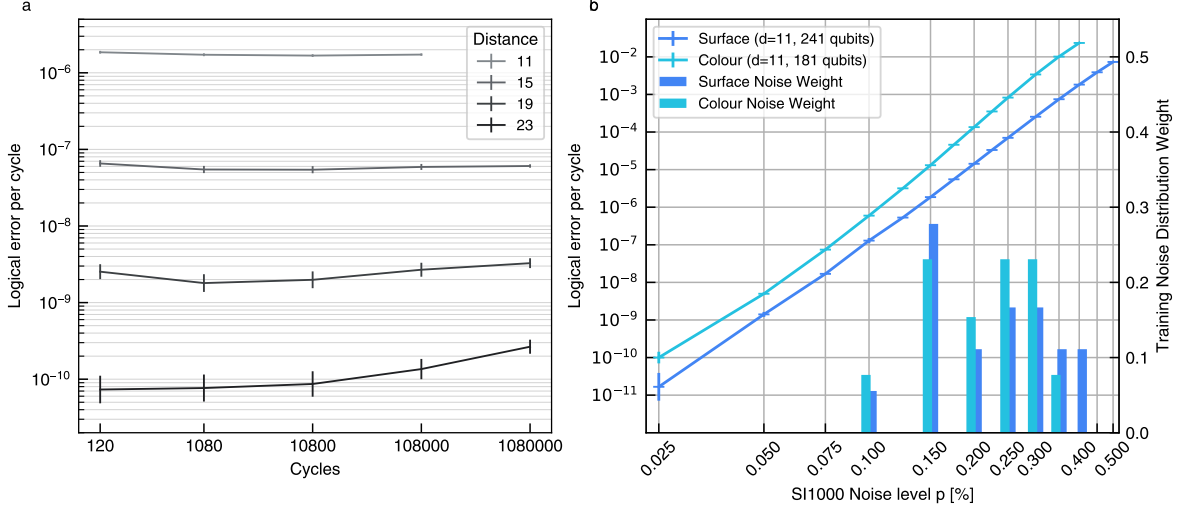


**Figure 5: Generalisation beyond the training distribution.** **a**, Decoding longer experiments. Decoding performance against number of cycles for AlphaQubit 2 measured on the surface code at code distances 11–23, with SI1000  $p = 0.15\%$  noise. The total number of shots used for evaluation increases with code distance (see Methods). For each code distance, the number of shots is decreased in inverse proportion to the shot length. **b**, logical error per cycle against noise level for distance-11 surface- and colour-code models (241 and 181 qubits). The bar plot represents the noise level distributions used during training.

## 6. Discussion and conclusion

In this work, we introduced AQ2, a neural-network decoder that addresses the dual requirements of high accuracy and real-time speed for quantum error correction. We have shown that this scalable architecture achieves near-optimal logical error rates for both the surface code and colour codes up to distance 23, matching or exceeding the accuracy of the best available decoders, and its time-invariant design was shown to generalize to million-cycle experiments, far exceeding the longest training example. Crucially, we demonstrated that a compact version of AQ2 meets the stringent  $1\ \mu\text{s}$  cycle time required for superconducting hardware for surface codes up to distance 11, using commercially available accelerators, and with minimal accuracy loss. The decoder’s performance was further validated on experimental data from a real-world quantum device, for which AQ2 (full and RT) had lower error rates than our strongest baseline. This reinforces the advantage of learning from data when decoding in the presence of correlations not captured by local Pauli error models.

While our results represent significant progress, several challenges remain. In terms of accuracy, we observed a deviation from ideal scaling at the highest distances, where training to convergence becomes more challenging, particularly for the colour code at distance 27 and in

million-cycle surface code experiments, indicating that further work on training methodologies for these regimes is needed. Reaching the logical error rates of  $10^{-12}$  and below needed for large-scale quantum applications is a further hurdle for which even reliable evaluation is a challenge, which will require increased computational resources or more sophisticated statistical estimation [44]. Although we achieved real-time throughput for distances up to 11, extending this capability to the larger distances required for full fault-tolerance will be the next major milestone. We anticipate that this can be achieved through a combination of further architecture innovation, algorithmic co-design, the use of low-precision arithmetic, and eventual implementation on specialized hardware (FPGAs, ASICs) as large-scale quantum devices become available (see Methods for an extended discussion). We have not yet addressed reducing the latency between the final measurement and the decoding result, whereas for many quantum computing applications it is critical to keep this to a minimum. Finally, while we have previously demonstrated the ability to decode logical operations (for the colour code [13]), integrating this capability at scale will be necessary for a complete fault-tolerant quantum computing stack.

In conclusion, AQ2 represents a substantial advance in quantum error decoding and demonstrates that neural decoders can satisfy the core requirements for fault-tolerant quantum computing. By providing a viable path to real-time neural decoding, our work addresses a critical bottleneck for leading error correction codes, while the model’s code-agnostic architecture opens the potential for discovering more efficient codes and protocols, accelerating the timeline towards practical quantum computers.

## References

- [1] S Lloyd. “Universal Quantum Simulators”. In: *Science* 273.5278 (Aug. 1996), pp. 1073–1078.
- [2] Stefano Pirandola et al. “Advances in quantum cryptography”. In: *Advances in optics and photonics* 12.4 (2020), pp. 1012–1236.
- [3] E Farhi et al. “A quantum adiabatic evolution algorithm applied to random instances of an NP-complete problem”. en. In: *Science* 292.5516 (Apr. 2001), pp. 472–475.
- [4] P W Shor. “Scheme for reducing decoherence in quantum computer memory”. en. In: *Phys. Rev. A* 52.4 (Oct. 1995), R2493–R2496.
- [5] Earl T Campbell. “Early fault-tolerant simulations of the Hubbard model”. In: *Quantum Sci. Technol.* 7.1 (Jan. 2022), p. 015007.
- [6] Ian D Kivlichan et al. “Improved Fault-Tolerant Quantum Simulation of Condensed-Phase Correlated Electrons via Trotterization”. In: *Quantum* 4 (Feb. 2019), p. 296.

- [7] Google Quantum AI. “Quantum error correction below the surface code threshold”. In: *Nature* 638.8052 (2025), pp. 920–926.
- [8] Austin G Fowler, Matteo Mariantoni, John M Martinis, and Andrew N Cleland. “Surface codes: Towards practical large-scale quantum computation”. In: *Phys. Rev. A* 86.3 (Sept. 2012), p. 032324.
- [9] H Bombin and M A Martin-Delgado. “Optimal resources for topological two-dimensional stabilizer codes: Comparative study”. In: *Phys. Rev. A* 76.1 (July 2007), p. 012305.
- [10] H. Bombin and M. A. Martin-Delgado. “Topological Quantum Distillation”. In: *Physical Review Letters* 97.18 (Oct. 2006). ISSN: 1079-7114. doi: [10.1103/physrevlett.97.180501](https://doi.org/10.1103/physrevlett.97.180501).
- [11] Craig Gidney, Noah Shutty, and Cody Jones. “Magic state cultivation: growing T states as cheap as CNOT gates”. In: *arXiv [quant-ph]* (Sept. 2024).
- [12] Google Quantum AI. “Suppressing quantum errors by scaling a surface code logical qubit”. en. In: *Nature* 614.7949 (Feb. 2023), pp. 676–681.
- [13] N Lacroix et al. “Scaling and logic in the colour code on a superconducting quantum processor”. en. In: *Nature* (May 2025), pp. 1–6.
- [14] Dolev Bluvstein et al. “Architectural mechanisms of a universal fault-tolerant quantum computer”. In: *arXiv preprint arXiv:2506.20661* (2025).
- [15] Yiqing Zhou et al. “Learning to decode logical circuits”. In: *arXiv [quant-ph]* (Apr. 2025).
- [16] Dolev Bluvstein et al. “Logical quantum processor based on reconfigurable atom arrays”. en. In: *Nature* (Dec. 2023).
- [17] Barbara M Terhal. “Quantum error correction for quantum memories”. In: *Reviews of Modern Physics* 87.2 (2015), p. 307.
- [18] Johannes Bausch et al. “Learning high-accuracy error decoding for quantum processors”. In: *Nature* 635.8040 (2024), pp. 834–840.
- [19] J Pablo Bonilla Ataides, Gu Andi, F Yelin Susanne, and D Lukin Mikhail. “Neural decoders for universal quantum algorithms”. In: *arXiv [quant-ph]* (Sept. 2025).
- [20] Moritz Lange et al. “Data-driven decoding of quantum error correcting codes using graph neural networks”. In: *arXiv:2307.01241* (2023).
- [21] Hanyan Cao, Feng Pan, Dongyang Feng, Yijia Wang, and Pan Zhang. “Generative decoding for quantum error-correcting codes”. In: *arXiv [quant-ph]* (Mar. 2025).
- [22] Zejun Liu, Anqi Gong, and Bryan K. Clark. *Decoding quantum low density parity check codes with diffusion*. 2025. arXiv: [2509.22347 \[quant-ph\]](https://arxiv.org/abs/2509.22347).
- [23] Gengyuan Hu, Wanli Ouyang, Chao-Yang Lu, Chen Lin, and Han-Sen Zhong. “Efficient and universal neural-network decoder for stabilizer-based quantum error correction”. In: *arXiv preprint arXiv:2502.19971* (2025).

- [24] Craig Gidney and Cody Jones. “New circuits and an open source decoder for the color code”. In: *arXiv [quant-ph]* (Dec. 2023).
- [25] Jack Edmonds. “Paths, trees, and flowers”. In: *Canadian Journal of mathematics* 17 (1965), pp. 449–467.
- [26] Austin G Fowler. “Optimal complexity correction of correlated errors in the surface code”. In: *arXiv:1310.0863* (2013).
- [27] Oscar Higgott. “PyMatching: A Python package for decoding quantum codes with minimum-weight perfect matching”. In: *arXiv:2105.13082* (2021). arXiv: [2105.13082](https://arxiv.org/abs/2105.13082) [quant-ph].
- [28] Oscar Higgott and Craig Gidney. “Sparse blossom: correcting a million errors per core second with minimum-weight matching”. In: *Quantum* 9 (2025), p. 1600.
- [29] Cody Jones. “Improved accuracy for decoding surface codes with matching synthesis”. In: *arXiv preprint arXiv:2408.12135* (2024).
- [30] Noah Shutty, Michael Newman, and Benjamin Villalonga. “Efficient near-optimal decoding of the surface code through ensembling”. In: (Jan. 2024). arXiv: [2401.12434](https://arxiv.org/abs/2401.12434) [quant-ph].
- [31] Yue Wu, Bingshong Li, Kathleen Chang, Shruti Puri, and Lin Zhong. “Minimum-weight parity factor decoder for quantum error correction”. In: *arXiv preprint arXiv:2508.04969* (2025).
- [32] Laleh Aghababaie Beni, Oscar Higgott, and Noah Shutty. “Tesseract: A search-based decoder for quantum error correction”. In: *arXiv [quant-ph]* (Mar. 2025).
- [33] Antonio deMarti iOlius, Patricio Fuentes, Román Orús, Pedro M Crespo, and Josu Etxezarreta Martínez. “Decoding algorithms for surface codes”. en. In: *Quantum* 8.1498 (Oct. 2024), p. 1498.
- [34] Christopher Chamberland and Michael E Beverland. “Flag fault-tolerant error correction with arbitrary distance codes”. In: *Quantum* 2 (2018), p. 53.
- [35] P Baireuther, M D Caio, B Criger, C W J Beenakker, and T E O’Brien. “Neural network decoder for topological color codes with circuit level noise”. In: *New Journal of Physics* 21.1 (Jan. 2019), p. 013003. doi: [10.1088/1367-2630/aaf29e](https://doi.org/10.1088/1367-2630/aaf29e).
- [36] Stergios Koutsoumpas, Tamas Noszko, Hasan Sayginel, Mark Webster, and Joschka Roffe. “Colour codes reach surface code performance using vibe decoding”. In: *arXiv [quant-ph]* (Aug. 2025).
- [37] Seok-Hyung Lee, Andrew Li, and Stephen D Bartlett. “Color code decoder with improved scaling for correcting circuit-level noise”. In: *arXiv [quant-ph]* (Apr. 2024).
- [38] Google Quantum AI. “Quantum supremacy using a programmable superconducting processor”. In: *Nature* 574.7779 (2019), pp. 505–510.
- [39] Craig Gidney, Michael Newman, Austin Fowler, and Michael Broughton. “A Fault-Tolerant Honeycomb Memory”. In: *Quantum* 5 (Dec. 2021), p. 605.

- [40] Craig Gidney. *How to factor 2048 bit RSA integers with less than a million noisy qubits*. 2025. arXiv: [2505.15917 \[quant-ph\]](https://arxiv.org/abs/2505.15917).
- [41] Craig Gidney. “Stim: a fast stabilizer circuit simulator”. In: *Quantum* 5 (July 2021), p. 497. ISSN: 2521-327X. doi: [10.22331/q-2021-07-06-497](https://doi.org/10.22331/q-2021-07-06-497).
- [42] C Ryan-Anderson et al. “Realization of Real-Time Fault-Tolerant Quantum Error Correction”. In: *Phys. Rev. X* 11.4 (Dec. 2021), p. 041058.
- [43] Google. <https://cloud.google.com/blog/products/compute/introducing-trillium-6th-gen-tpus>.
- [44] Carolyn Mayer et al. *Rare Event Simulation of Quantum Error-Correcting Circuits*. 2025. arXiv: [2509.13678 \[quant-ph\]](https://arxiv.org/abs/2509.13678).

## Acknowledgements

We thank Aria Shahingohar, Borislav Kozlovskii, Craig Donner, Laleh Beni, Sebastian Bodenstein, Sebastian Nowozin, and Stig Petersen for their support and contributions to the project, and Alex Gaunt, Ryan Babbush and Vlad Sivak for further feedback on the paper. We thank Demis Hassabis for sponsoring the research and creating the environment that made this work possible.

## Author contributions

These authors contributed equally: Andrew W. Senior, Thomas Edlich, Francisco J. H. Heras, Johannes Bausch. J.B., T.E., A.W.S. and F.J.H.H. contributed to conceptualization and methodology, software, engineering, experimentation, formal analysis and writing. O.H., M.N., C.J., N.S., J.L. and P.B. contributed to QEC theory, decoding methodology, and baselines. L.Z., J.S., O.H., M.N., C.J., N.S., S. Blackwell and S. Boixo contributed to paper review. L.Z., J.S., T.A. and Y.L. contributed to software, engineering and experimentation. J.B., M.N., C.J., S.B., A.D., H.N. and P.K. contributed to project supervision. A. Žemgulytė, A. Žídek, A.C., C.B. and S. Blackwell provided software and engineering support. G.H. contributed to project administration.

## A. Data availability

The Willow data used here is available at <https://doi.org/10.5281/zenodo.14238944>. All other data was sampled from the Stim simulator.

## B. Methods

### B.1. Network Architecture

#### B.1.1. Full AlphaQubit 2 architecture

The AlphaQubit 2 (AQ2) architecture is a new architecture for predicting logical observables from stabilizer measurement events. It shares some attributes with AlphaQubit 1 (AQ1 [18]) —a per-stabilizer representation; recurrency; the use of transformers; and a readout network with pooling—but is fundamentally different (Figure 1). In particular, instead of the transformer computation being inside the recurrent processing block, we now adopt a light-weight recurrent layer (Figure S1b) which we interleave with transformer layers (Figure S1a). This has advantages for inference speed, since now, at inference time, the transformer operations can be carried out in parallel across a number of cycles leading to more efficient use of the computing accelerator and thus greater throughput. For simplicity and uniformity of the architecture across code types, we use no convolutions and replace the readout network’s pooling from a data qubit representation with a simple mean pooling across stabilizers, with a separate embedding per-logical observable and cross-attention between the logical observable representations and the final per-stabilizer representation. By training the network on the binary logical observable, the network outputs an estimate of the probability of the logical observable being 1.

Instead of processing one cycle in each time step, to improve inference and training speed, we combine multiple (6 for simulated surface code, 3 for simulated colour code, 5 for the Willow data) cycles of measurements, and run the network at a correspondingly lower rate. The final cycle of syndrome measurements in each experiment, derived from measuring the data qubits, is embedded by itself but processed with the same network. The new architecture accumulates groups of cycles of measurements before temporally compressing them (by concatenating and projecting the vector embeddings) and feeding the combined representation through a series of spatial or temporal network layers. The spatial layers are transformer layers that implement self-attention between the stabilizer representations (independently at each time step). The temporal layers are recurrent layers that integrate new information from a lower layer into a recurrent network state (independently for each stabilizer). At the end of an experiment, the

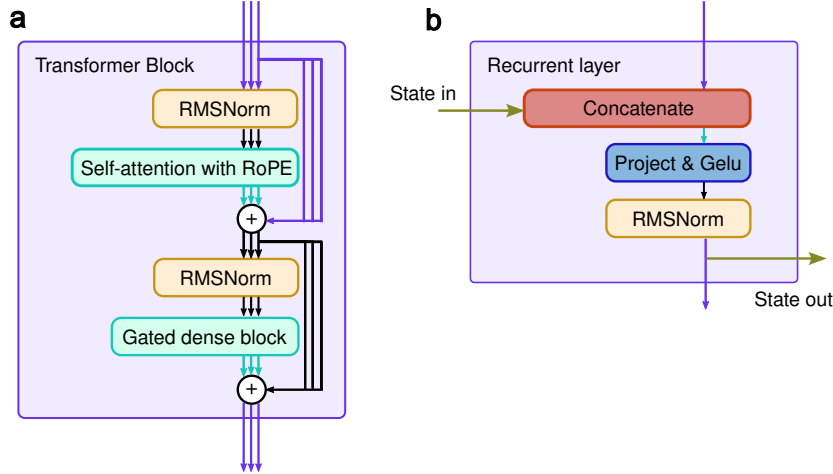


Figure S1: **Components of the AlphaQubit 2 architecture.** **a**, Spatial mixing transformer block operating on all stabilizer representations at one time step. **b**, Recurrent layer for each stabilizer.

final cycle of stabilizers is processed with the same network stack and the output from the final layer is supplied to the readout network to make a label prediction for each logical observable.

For the full-sized AQ2, optimized for accuracy (AQ2-full), the recurrent layers (RNNs, Fig. S1b) combine the previous state and the layer’s inputs for the current cycle by concatenating them and projecting to the original dimension. The projection is followed by a Gelu activation [45] and an RMSNorm layer [46]. The RNN output is used both to feed to the next layer and as the state for the next time step. Better training was observed by initializing the weights that project the state to a random orthogonal matrix. Each state is initialized with the zero vector at the start of an experiment. In the speed-optimised version of AQ2 (AQ2-RT) we used a faster, element-wise gated recurrence (See B.1.5 for details).

The spatial mixing transformer layers (Fig. S1a) consist of an RMSNorm normalization followed by multiheaded self-attention between the stabilizer embeddings, with a parallel residual connection. A further normalization followed by a gated dense block computes a further update to the residualized activations.

For AQ2-full we use the following layer sequence, as shown in Fig. S2:

RNN; RNN; 3 transformer layers; RNN; 3 transformer layers; RNN;  
3 transformer layers; RNN

The readout network combines the final per-stabilizer representation by mean-pooling. We replicate this representation for each logical observable being predicted (only one in inference) and add a learned embedding to each. The per-logical observable representations cross-attend to the final per-stabilizer representation.

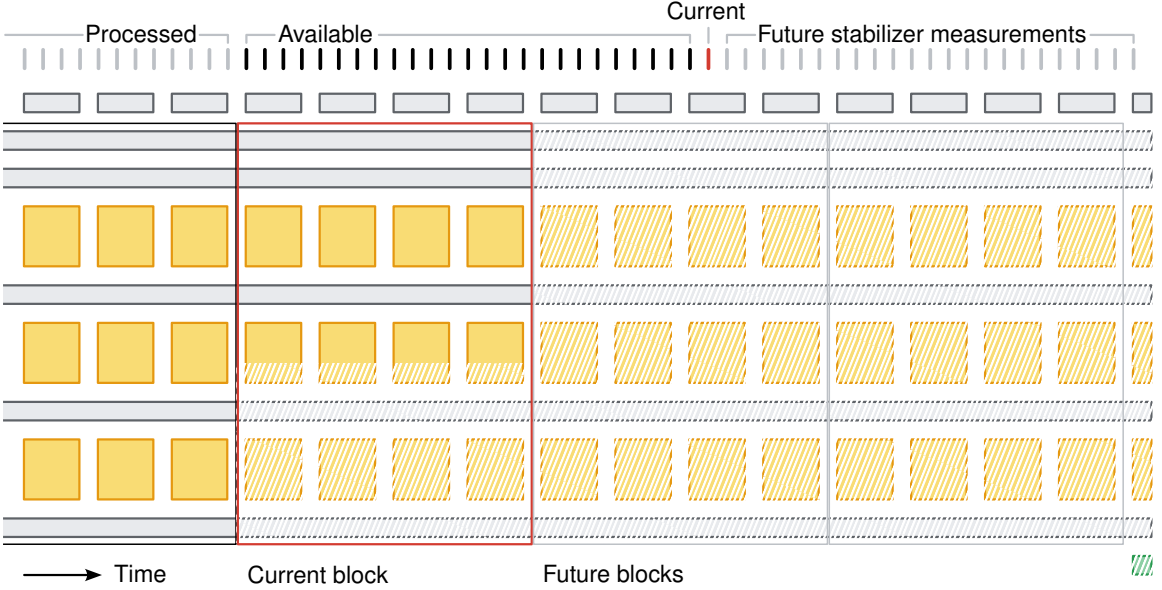


Figure S2: **Neural network layers for one time block of cycles.**

After two cross-attention transformer layers, each logical-observable representation is processed by two residual dense layers before projecting to a single channel and logistic activation function.

### B.1.2. Embedding

AQ2 uses a variety of embedding methods.

Stabilizers are embedded with a linear embedding. For the surface code we add the embeddings of both measurement and events for each stabilizer, and for the colour code we add the embeddings of measurements and the corresponding flags (See B.3.4). We also add a normalized position encoding for each of  $x$  and  $y$ , which linearly embeds the normalized coordinates of each qubit relative to the current code patch size. Thus, for the surface code, regardless of code distance, the left (right) edge always has an  $x$  coordinate of -0.5 (0.5).

For spatial self-attention we use Rotational Position Encodings (RoPE [47]) of the spatial coordinates of the physical qubits. Half of the channels use the  $x$  coordinate and half use the  $y$  coordinate. For the colour code X & Y basis measurements occur at the same physical location, so we add a basis embedding vector learned for each basis. After pooling for the readout network, we add a separate learned embedding for each of the logical observables to disambiguate them for the cross-attention.

### B.1.3. Ensembling

In AQ1 we showed that even better accuracies can be obtained by combining the error estimates of multiple models with no time penalty, at the cost of additional hardware to parallelize the model evaluations. The same technique can be applied to AQ2. For simplicity, most results use a single model and we only use ensembling to achieve peak performance at the highest distances (Table S2), and with the Willow experimental data, where we follow our previous protocol [7] in which we ensemble 5 similar models trained with different random seeds.

For the surface code at distance 23, we ensemble a base model trained with code distances up to 23 with the same model further fine-tuned at distance 23. We note that the fine-tuned model achieved slightly higher accuracy at 120 cycles, but did not generalize as well to higher code distances. For the colour code we ensembled fine-tuned variants of the base model: two at distances 19 and 23, and three at distance 27. We would expect some improvement in all the results by ensembling where a single model was used, or increasing the size of the ensemble, but expect that most of the gains have been realised. With distillation [48] it may be possible to train a single “student” model which achieves similar performance to the ensemble and thus avoid the additional computational burden.

### B.1.4. Principal architecture differences compared to AlphaQubit 1

The principal differences between the AQ1 architecture and that used here for AQ2-full are as follows:

- Adoption of the layer-based architecture with light-weight RNN layers (Figure S1b), rather than the processing all being carried out within a large RNN core.
- Temporal compression of consecutive frames before processing.
- No convolutions.
- Use of cross-attention at the start of the readout network.
- Use of spatial RoPE.

### B.1.5. Architecture changes for Real-time AlphaQubit 2

To achieve throughput of under  $1\mu\text{s}$ , we train smaller models (AQ2-RT) with the following variations:

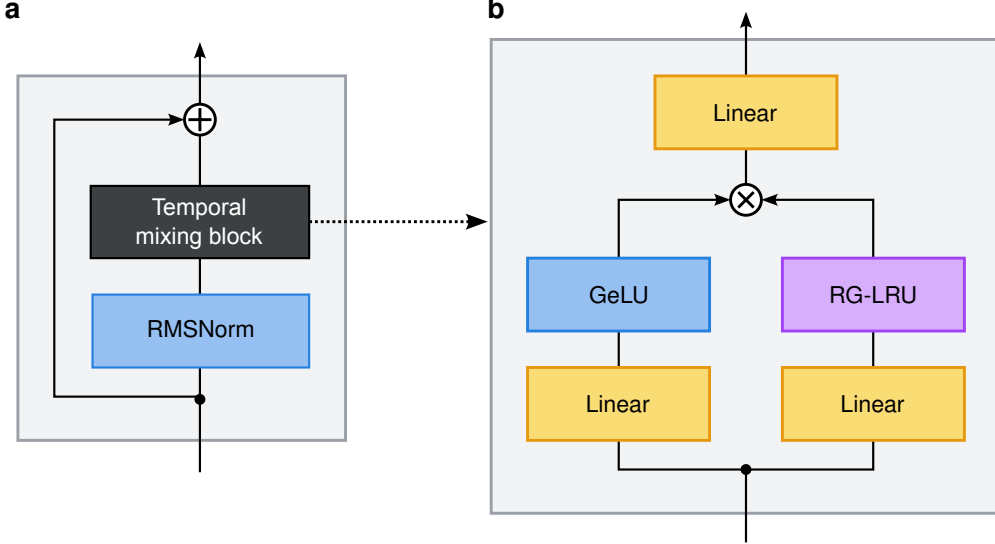


Figure S3: **Gated recurrence RNN layers.** **a**, residual block. **b**, recurrent block.

- The layer sequence is:
  - 1 RNN layer, 3 transformer layers; 1 RNN layer (Willow experiments) or 1 RNN layer, 2 transformer layers; 1 RNN layer (Scaling experiments).
- The readout layer has 2 spatial mixing transformer layers before the readout network described above.
- The internal representation per stabilizer has 128 channels (256 for Willow experiments).
- The RNN layers use a gated recurrence [49], which is faster because it only involves element-wise operations (Fig. S3).

For the Willow data which has durations with multiples of 10 cycles, we temporally compressed groups of 5 cycles instead of 6.

## B.2. Training

While AQ1 used a combination of pretraining on synthetic noise and fine-tuning on experimental data (simulated for larger code distances), since the focus here is on scaling to surface code sizes well beyond current hardware, we conduct the scaling experiments using SI1000 and train in a single phase without the need for fine-tuning. For the Willow data, we follow the same protocol as used in the Willow paper of training five models for each code distance on SI1000, fine-tuning on samples taken from a Detector Error Model (DEM) fitted to experimental data,

followed by a final fine-tuning using the limited experimental samples while holding out a test set of experimental samples (as well as an evaluation set to monitor fine-tuning progress).

We train our models on examples from a range of code-distances. A fully-trained model is able to decode examples from any of the distances seen in training. For ease of training, we follow a code distance curriculum, where we change the distribution of samples over time, initially focusing on the smaller code distances and finishing by focusing on larger code distances. While this allows us to more quickly achieve high accuracy for larger code distances, and avoids separate training for each code distance, maintaining performance across all code distances does involve sacrificing a small amount of accuracy. We train two models for each code — one only up to distance 11 and the other for higher distances. To achieve the best performance for the colour code at distance 23, we conduct final training only on distance 23 examples, resulting in a network specialized for just that code distance. To extract the absolute best performance, it would be possible to carry out such fine-tuning for each code distance, but here we just focus on the highest code distance where the focused training makes the greatest difference.

We note that for the surface code at distance 23, we achieve an LER of around  $7.3 \times 10^{-11}$ , but only see  $3 \times 10^9$  training examples or  $3.6 \times 10^{11}$  cycles, so we expect to see very few incorrect examples in the latter half of training, but the cross-entropy objective leads to beneficial gradients from the correctly classified examples.

### B.2.1. Noise

While for all the simulations we target a noise level of  $p=0.15\%$ , we find it beneficial to train with a mixture of harder and easier examples, and it is easier for the model to learn with examples with a lower noise level. We generate each training example with a noise level sampled from a distribution (see Table S1).

### B.2.2. Masking

We find that training the model with dropout on the inputs (akin to that used in BERT [50]) leads to better results. We drop out 50% of stabilizer representations in each cycle, replacing them with zero-vectors. We do so on only 80% of training examples to ensure that the model sees examples with all stabilizer representations (as are used in inference).

### B.2.3. Auxiliary losses

During training we predict a number of auxiliary losses to improve the speed of conversion and to push the network to decode at any shot length (See B.3.3). As in AQ1 we can predict multiple

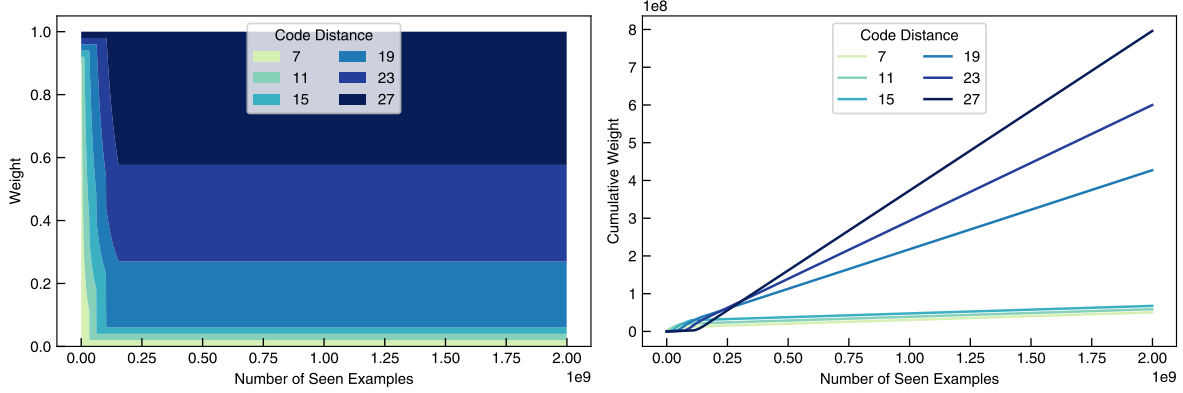


Figure S4: **Code distance curriculum.** Shown are weights (left) and the cumulative number of samples seen (right), over a period of  $2 \times 10^9$  total training samples.

logical observables for the logical qubit for any experiment, and by simulating terminating the experiment at any cycle, with a set of data qubit measurements at each cycle, we train the network to predict these logical observables at every cycle. Furthermore, we simulate such logical observables in each basis but using separate parameters in the readout network.

#### B.2.4. Code distance curriculum

We use a code distance curriculum which gradually increases the weight on larger code distances as training progresses. The weights and cumulative number of samples seen over a 2B training run can be seen in Fig. S4.

#### B.2.5. Optimization

We generally use the Lion optimizer [51]. For fine-tuning we adopted the Muon optimizer [52]. We use a batch size of 1024 throughout, apart from the finetuning runs on Willow data for which we used a batch size of 64 ( $d = 3$ ), 128 ( $d = 5$ ), or 256 ( $d = 7$ ).

#### B.2.6. Learning rate

We have a 1-million example linear warm-up period to reach the full learning rate and use a fixed learning rate throughout training with an optional cosine decay, particularly for fine-tuning (Table S1, Table S2).

We scale the learning rate for each batch according to the code distance and number of cycles with the following formula:

$$\text{learning\_rate} = \text{base\_learning\_rate} \times 0.8^{\log_2 N_s/8} \times 2^{\log_2 R/24}$$

Parameter	Surface		Colour	
Training code distances	3, 5, 7, 9, 11	7, 9, 11, 13, 15, 17, 19, 21, 23	3, 5, 7, 9, 11	7, 11, 15, 19, 23, 27
Evaluation code distances	3, 5, 7, 9	11, 15, 19, 23	3, 5, 7, 9	11, 15, 19, 23, 27
cycles for training	24, 48, 72, 120	24, 48, 72, 120	24, 48, 96, 120	120
Parameters	32,177,930	32,177,930	68,514,592	29,539,186
Channels	512	512	512	512
Heads / key size / value size	16 / 32 / 32	16 / 32 / 32	32 / 32 / 64	16 / 32 / 32
Widening	4	4	8	4
Pooling transformer layers / heads / key & value size	4 / 8 / 32	4 / 8 / 32	8 / 8 / 32	2/8/32
Total training examples	2e9	2e9	2e9	7.0e8
Noise distribution ( $p$ , relative weight)	(0.001, 1), (0.0015, 5), (0.002, 2), (0.0025, 3), (0.003, 3), (0.0035, 2), (0.004, 2))	(0.001, 1), (0.0015, 5), (0.002, 2), (0.0025, 3), (0.003, 3), (0.0035, 2), (0.004, 2)	(0.001, 1), (0.0015, 2), (0.002, 7), (0.003, 3)	(0.001, 1), (0.0015, 6), (0.002, 4), (0.0025, 3), (0.003, 2), (0.0035, 1)
Learning rate	2e-5	2.2e-5	2.4e-5	2.5e-5
Learning rate decay factor	—	—	0.25	—
Decay examples range	—	—	1.2e9 to 2e9	—

Table S1: Model and training hyperparameters for the four base models.

where  $N_s$  is the number of stabilizers in the example at the given code distance and  $R$  is the number of cycles. (Double the number of cycles for the colour code).

Parameter	Surface	Colour		
Code distances	23	19	23	27
Cycles for training	72, 120, 168	120	72, 120, 168	120
Total training examples	$3 \times 10^9$	$9.5 \times 10^8$	$3 \times 10^9$	$1.3 \times 10^9$
Muon learning rate	$2.5 \times 10^{-3}$	$4 \times 10^{-4}$ $1 \times 10^{-3}$	$2.5 \times 10^{-3}$	$1.0 \times 10^{-3}$ $1.5 \times 10^{-3}$ $2 \times 10^{-3}$
Ensemble	Base model with 1 finetune	2 finetunes	2 finetunes	3 finetunes
Ensemble $\log_{10}$ LER	-10.135	-8.052	-9.456	-10.398
Model $\log_{10}$ LERs	-10.079 -9.778	-7.714 -7.764	-8.589 -8.530	-8.127 -8.233 -8.474
Learning rate decay factor	0.2	0.25	0.1	0.25
Decay examples range	2e9 to 3e9	5.6e8 to 1e9	7e8 to 2.3e9	5.6e8 to 1e9

Table S2: **Fine-tuning hyperparameters for the variants used in ensembles.**

## B.3. Data

For our standard evaluations we chose 120-cycle memory experiments to have durations longer than  $d \times 3$  for all code distances, and retaining flexibility in choosing the group length for temporal compression.

### B.3.1. Circuits

All surface code data is generated from a XZZX surface code with the same readout ordering as in our previous work [18], see Fig. S5a.

Our Bell-flagged colour code implementation follows Baireuther [54], see Fig. S5b. We note here that the graph defined by pairs of stabilizer and data qubits connected by 2-qubit gates in the readout circuit is not planar, which means it is not directly implementable on a substrate with planar qubit connectivity, but which could e.g. be run on a device with all-to-all connectivity, such as a neutral atom device. Other readout orders [24, 55] are planar and thus directly suitable for superconducting chips. We only found minor accuracy differences between these Bayreuther-style circuits and e.g. those implemented in Gidney et al. [24], the latter potentially giving a slight edge in accuracy.

Due to the impossibility of running Chromobius in our colour code implementation, we measured its performance on superdense colour code circuits of the same size and noise model. The readout ordering follows Gidney et al. [24].

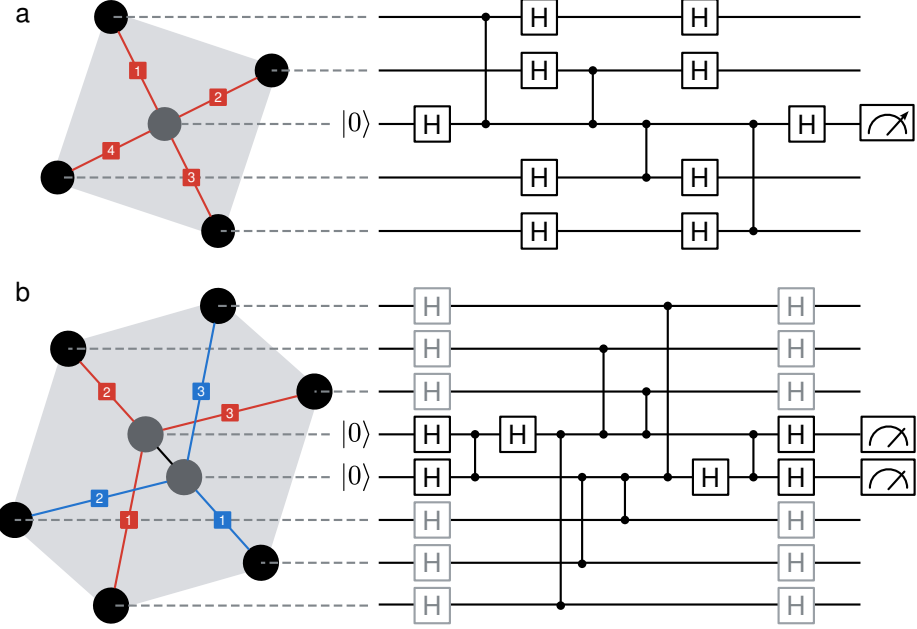


**Figure S5: Readout circuits and topology for surface and colour codes.** **a**, Common X and Z stabilizer readout for the XZZX rotated surface code [53]. For an adjacent plaquette, the readout order is anti-clockwise s.t. data qubits are touched in a consistent order for overlapping stabilizers. **b**, Stabilizer readout for Bell flagged colour code [35], where the grey Hadamard gates are applied for an X readout, and not for a Z readout. The topology is non-planar as the CZ gates applied between ancilla and data qubits cross.

### B.3.2. Circuit level noise

We use SI1000 [56] (superconducting-inspired 1,000-ns cycle duration) noise in our simulations. (See Figs. S6 and S7 for full circuit details.) SI1000 is a circuit depolarising noise model that approximates the noise processes occurring in superconducting circuits. We note that there was some ambiguity in the original definition [39] of SI1000, now resolved [57]. In this work we fully align with the modern interpretation, which is different from the SI1000 interpretation used in our previous work [18] in two ways: Both  $\text{Idle}(p) = p/10$  and  $\text{ResonatorIdle}(p) = 2p$  noise terms are added after measurements and resets (instead of just  $\text{ResonatorIdle}(p)$ ). Measurement and reset count as two separate operations with full sets of noise applied (instead of a joint operation with a single set of noise) This produces a minor increase in events at each particular value of  $p$ .

Example noise in measurement-and-reset stabilizer qubits in old and new SI1000 interpretation. Before (AQ1 [18]):

```
X_ERROR(0.01) 7 8 9 10 11 12      # 5p pre-measurement noise
```

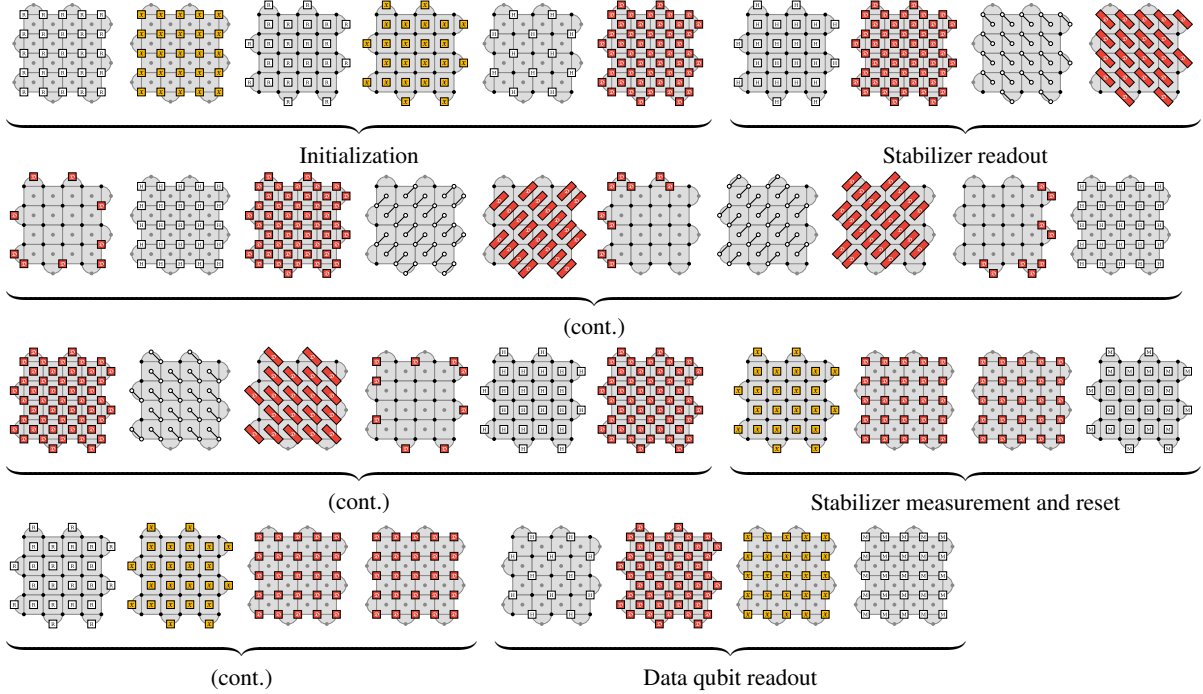


Figure S6: **Circuit sequence for the surface code.** Bit flip errors are denoted in yellow, depolarizing channels in red. CZ gates are marked with their circuit symbol. Measurement, reset, and Hadamard gates are marked with an M, R, and H, respectively.

```

MR 7 8 9 10 11 12
X_ERROR(0.004) 7 8 9 10 11 12      # 2p post-measurement noise
DEPOLARIZE1(0.004) 0 1 2 3 4 5 6 # 2p ResonatorIdle noise

```

In this work:

```

X_ERROR(0.01) 7 8 9 10 11 12      # 5p pre-measurement noise
M 7 8 9 10 11 12
DEPOLARIZE1(0.0002) 0 1 2 3 4 5 6 # p/10 further measurement idle noise
DEPOLARIZE1(0.004) 0 1 2 3 4 5 6 # 2p Idle noise (due to measurement)
R 7 8 9 10 11 12
X_ERROR(0.004) 7 8 9 10 11 12      # 2p Post-measurement noise
DEPOLARIZE1(0.0002) 0 1 2 3 4 5 6 # p/10 Idle noise
DEPOLARIZE1(0.004) 0 1 2 3 4 5 6 # 2p ResonatorIdle noise (due to reset)

```

### B.3.3. Intermediate data

When simulating data, we have some privileged information about quantum states, which would be inaccessible in a real experiment due to the no-cloning theorem. We use this privileged

information to provide the model with some auxiliary labels at each experiment step. There are two types of intermediate auxiliary information.

**[fake endings]** Fake alternative endings of the experiment at every cycle. We calculate them by measuring the data qubits and deriving a fake alternative last cycle of stabilizer measurements and observables.

**[noiseless observables]** We use MPP (multi-pauli instructions) measurements on the data qubits in the observable line, to obtain a noiseless measurement of the observable at each cycle. We entangle it in a bell pair to provide a result also for an orthogonal measurement basis.

We calculate each intermediate observable for a number of equivalent measurement lines. For the surface code we choose each vertical (resp. horizontal for X experiments) line of data qubits, giving us code-distance bits per intermediate observable. For the colour code we chose the data qubits in each of the three sides of the triangular patch, giving us 3 bits per intermediate observable.

We combine these two sources of intermediate measurements to provide the model with 4 intermediate labels at each cycle:

**[fake intermediates]** We use an extra head at each group of cycles that receives the fake ending stabilizer measurements to predict the fake ending observables.

**[noiseless]** An extra head at each time step predicting the noiseless observable at each time chunk

**[noiseless delta]** An extra head at each time step predicting the xor (exclusive or) between two noiseless observables at the beginning and end of each time chunk.

**[noiseless to intermediate delta]** An extra head at each time step that receives the fake ending stabilizer measurements to predict the xor between a noiseless observable at the beginning of the time chunk and a fake ending observable at the end of the time chunk.

Each label is used in optimization as an auxiliary binary cross-entropy loss. During training we balance these auxiliary losses and the final loss by optimising a weighted sum of the losses (see weights in Table S3). During evaluation, we do not need to make predictions from any auxiliary heads. To minimize bugs, the held-out test data used to calculate the final reported accuracies is in all cases calculated from a simple circuit and data pipeline that never generates any intermediate measurements nor labels.

Loss	Weight
Final	1.2
Fake intermediate	1
Noiseless	1
Noiseless delta	1
Noiseless to intermediate delta	8

Table S3: Loss weights

#### B.3.4. Unified data representation

In the Bell-flagged colour code, stabilizer and flag qubits are measured in alternating bases in two sub-cycles. Thus the measurements at a given physical location have two different meanings. To make a representation more consistent with that of the surface code, with spatial consistency, we reshape the two sub-cycles into a single cycle representation. The X and Z basis stabilizer measurements are interleaved, to make a unified representation for the cycle. The flag measurements are similarly interleaved, aligned with the stabilizer measurements. When using the unified representation we combine only 3 consecutive cycles of information before presentation to the neural network.

#### B.3.5. Willow experimental data

For the experimental data experiments we use the data from the Willow paper [7] and follow the same protocol. The data consists of 50,000 shots of training data for each duration  $\{10, 30, 50, \dots, 250\}$  cycles for each distance  $\{3, 5, 7\}$  and in each basis  $\{X, Z\}$ . Distance 3 and 5 datasets are taken at each of 9 and 4 locations, respectively, on the 105-qubit Willow chip. A Detector Error Model (DEM) fitted to data from a separate 13-cycle dataset at each distance was used for the initial fine-tuning, and an RL-modified DEM was used by the matching decoder. For the final fine-tuning we do two-fold cross validation, splitting each set into two parts. One half is used for final evaluation and the other split into 19,880 fine-tuning examples and 5,120 evaluation examples to measure the progress of fine-tuning.

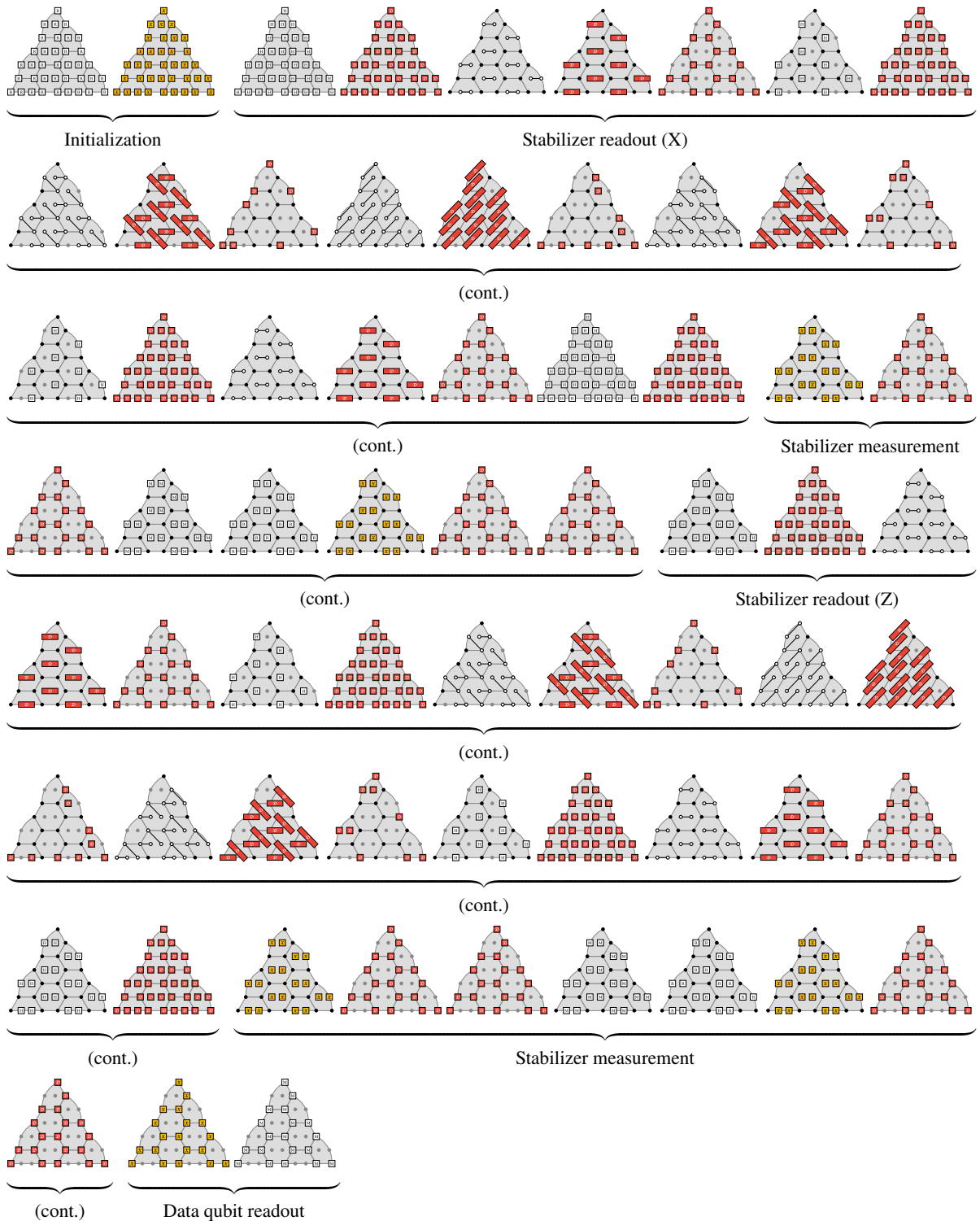


**Figure S7: Circuit sequence for the Bell-flagged colour code.** Bit flip errors are denoted in yellow, depolarizing channels in red. CZ gates are marked with their circuit symbol. Measurement, reset, and Hadamard gates are marked with an M, R, and H, respectively.

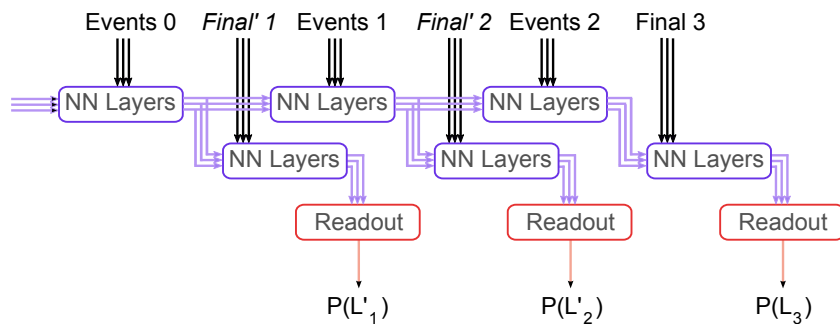


Figure S8: **Fake endings.** By simulating early terminations of an experiment we can measure final data qubits, give the network the corresponding final stabilizers and thus predict a logical observable  $L'$  for each cycle of an experiment in addition to the final logical observable  $L$ .

## B.4. Measuring accuracy

Accuracy is measured with logical error per cycle (LER).

For evaluating on shots of a single length  $n$  cycles, of which a fraction  $E(n)$  are incorrectly decoded, we compute  $\text{LER} = \frac{1}{2}(1 - \sqrt[n]{1 - 2E(n)})$ . For the experimental data, with test data of various durations, we fit a straight line to the log fidelities

$$F(n) := 1 - 2E(n) :$$

$$\log F(n) = \log F_0 + n \log(1 - 2\epsilon),$$

following [7].

A cycle is defined here to involve the measurement of the stabilizers in both bases, so for the Bell-flagged colour code this involves measuring all the stabilizer and flag qubits twice (for X and Z basis sequentially, Fig S7). Therefore with the same clock-speed a cycle in the colour code will take about twice as long as for the surface code. This is an approximation, as the readout circuits are different, for instance associating each stabilizer with 3 data qubits in the colour code and 4 in the surface code (Fig S5).

We measure the accuracy of the decoders on a fixed, held-out dataset of examples from Stim. These datasets were only used for final evaluation of the selected model of each configuration. Since higher code-distance decoders have lower error rates, we require larger test sets to accurately estimate the error rates. The number of samples used for each code distance for each code is shown in Table S4. We used independent large benchmarking datasets of the same sizes to compare between models trained with different hyperparameters and to make the final selection of which model to evaluate with the held-out test set.

The number of samples was chosen to achieve reasonable error bars for the LER at the expected LER for each code distance. During development we use separate temporary development datasets to monitor the training of the networks and determine when to finish

Code distance	Samples for Surface Code	Samples for Colour code
3	500,000	500,000
5	2,000,000	1,500,000
7	5,000,000	3,000,000
11	10,000,000	6,000,000
15	50,000,000	25,000,000
19	250,000,000	250,000,000
23	2,500,000,000	500,000,000

Table S4: **Numbers of samples used in evaluations.** For the SI1000 0.15% benchmarking and final, held-out test sets, by code distance (for 120-cycle shots).

Code distance	cycles				
	120	1,080	10,800	108,000	1,080,000
11	10,000,000	1,125,000	125,000	25,000	25,000
15	50,000,000	5,575,000	575,000	75,000	25,000
19	250,000,000	27,800,000	2,800,000	300,000	50,000
23	2,500,000,000	277,800,000	27,800,000	2,800,000	300,000

Table S5: **Numbers of samples used in evaluations.** For the SI1000 0.15% benchmarking and final, held-out test sets for long experiment evaluations, according to number of cycles.

Code distance	Samples for Surface Code	Samples for colour code
3	5,000,000	5,000,000
5	20,000,000	15,000,000
7	50,000,000	30,000,000
11	100,000,000	60,000,000
15	500,000,000	250,000,000
19		2,500,000,000

Table S6: **Numbers of samples used in held-out test set for 0.1% noise.**

training. Evaluation on datasets of the above sizes is too expensive, particularly for larger code distances where examples are more expensive to evaluate, as well as requiring larger test sets to estimate error rates accurately. To achieve faster evaluation with sufficiently low standard error, we evaluate on data with much higher noise, for which the error rate is correspondingly higher and evaluation requires fewer samples. For the surface and colour codes we use  $p = 0.3\%$  and  $p = 0.25\%$  noise respectively. While improving performance on the high noise data is no guarantee of improving performance at the target 0.15% noise level, this is a useful proxy which makes preliminary model comparison much less compute-intensive.

#### B.4.1. Long experiment datasets

To benchmark surface code decoders on longer experiments, we decrease the number of samples used in proportion to the increase in duration (Table S5). Numbers of rounds are chosen to be multiples of 24 (using a group size of 6 cycles and a block size of 24 or 48).

#### B.4.2. Low noise samples 0.1% noise

To measure error rates at 0.1% noise, we use 10 $\times$  more samples than for 0.15% noise (Table S6).

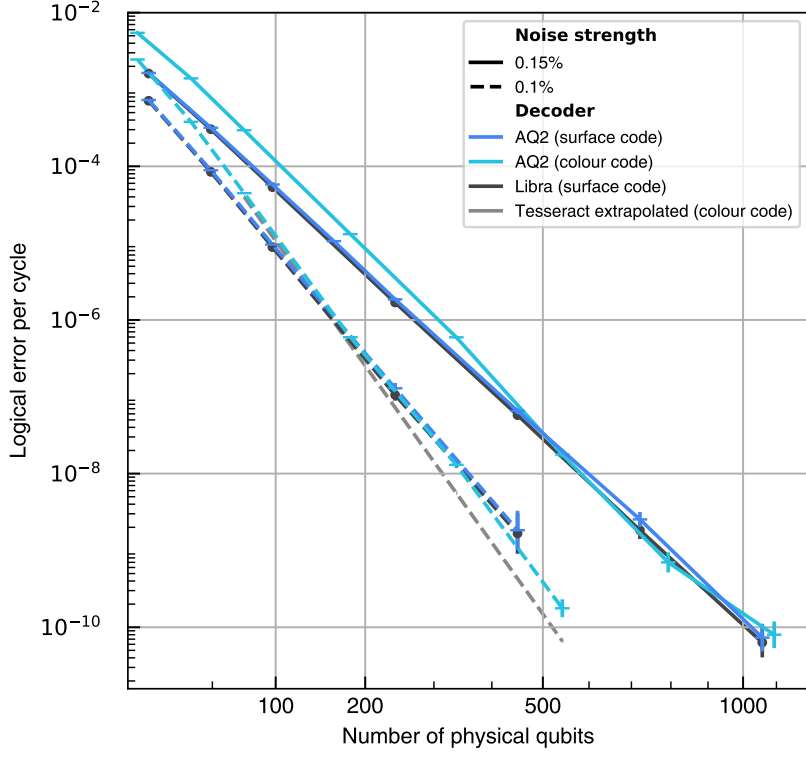


**Figure S9: Comparison between codes.** Logical error per cycle versus number of physical qubits for AQ2, comparing colour and surface decoding at 0.15% and 0.1% noise, together with Libra and (at 0.1%) extrapolated Tesseract baselines.

#### B.4.3. Comparing AQ2 across codes

By plotting the logical error rates of Fig. 3a & b, as well as the corresponding rates for 0.1% noise, against the number of physical qubits required to implement the different codes, we can see (Fig. S9) that the accuracies for colour and surface code at these noise levels are comparable. The decoders scale well at the lower noise level, matching the accuracy of Libra on the surface code and coming close to the extrapolated Tesseract error rate, confirming the noise generalization shown in Fig. 5b.

#### B.5. Measuring speed

We measure throughput and latency of AQ2 models on a Trillium TPU. The model is executed in a streaming fashion where the decoder accumulates a block of cycles before processing them jointly. While the model is executed on a block, new cycles are accumulated into a buffer. At the end of the memory experiment, the readout network is executed to get the final prediction. In order to measure throughput, we measure the duration from the experiment start to when the

final prediction is complete and divide by the number of cycles:

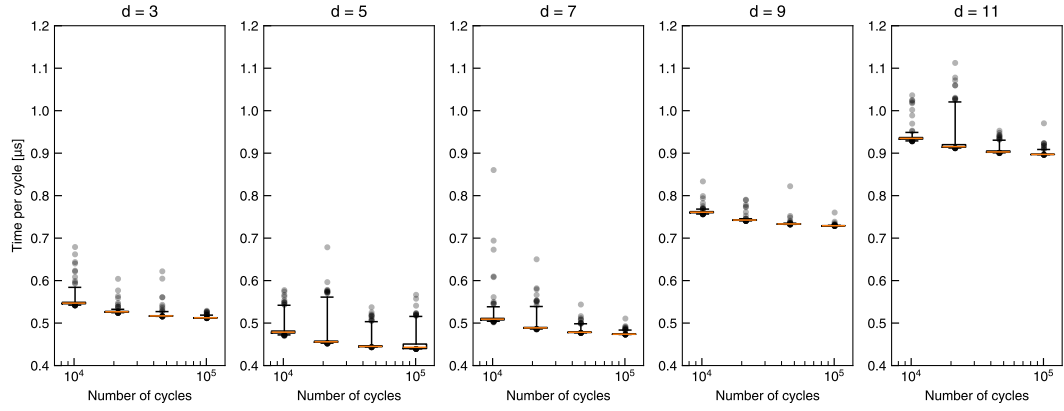
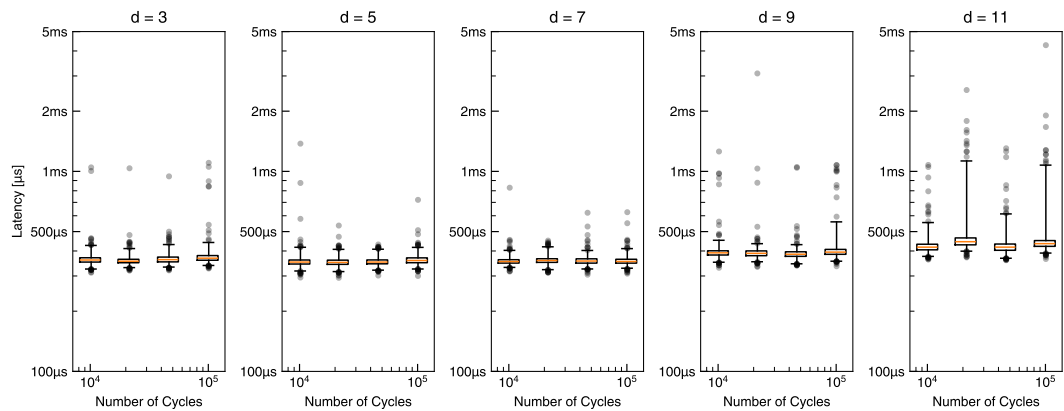
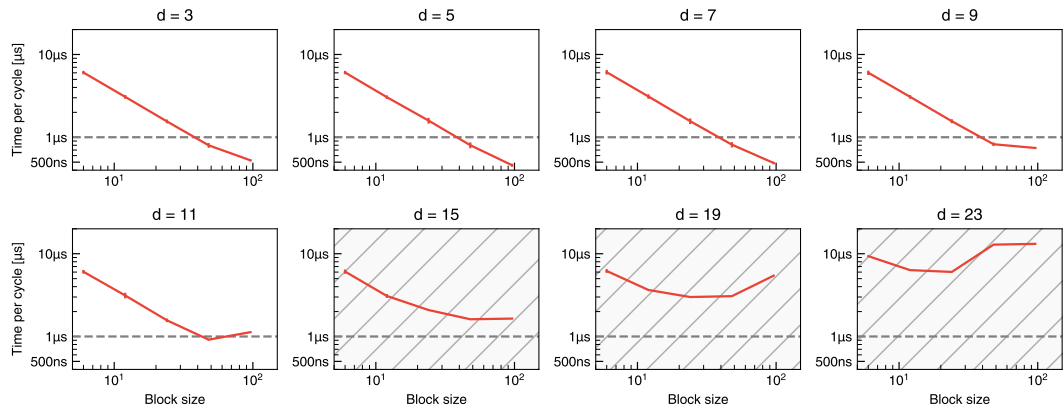
$$\text{throughput} := \frac{\text{duration}}{\text{num\_cycles}}$$

We choose a large number of cycles (100,800) to approximately cancel out constant effects on timing such as executing the final readout network. All timing is carried out with a single memory experiment at a time, but we note that, for lower code distances, multiple logical qubits can be decoded in parallel on a single device within the throughput, amortizing the compute hardware requirement.

We measure latency by introducing a simulated clock rate such that the decoder receives the measurements of a single cycle at a fixed frequency, e.g. every 1  $\mu\text{s}$ . The latency of a decoder is then defined as the delay between receiving the last cycle and the prediction being ready:

$$\text{latency} := \text{time\_prediction\_done} - \text{time\_last\_cycle}$$

We show in Figure S10 that the latency of AQ2-RT remains constant for increasing numbers of cycles[7], showing that the decoder can keep up with the simulated clock rate of 1  $\mu\text{s}$ . It should be noted that the throughput and latency of AQ2 are independent of the detection fraction and the error pattern, unlike matching-based decoders whose runtime increases with error density and can have extreme worst-case decoding times that necessitate lower-accuracy fall-back mechanisms.

**a****b****c**

**Figure S10: Throughput and latency measurements.** **a, b**, Box plots of decoding time per cycle (**a**) and latency (**b**) for different code distances and memory experiment lengths. Each plot represents 1000 shots of 100,800 cycles with whiskers extending from 1st to 99th percentile. Latencies are measured with a simulated cycle time of 1  $\mu\text{s}$ . **c**, Average time per cycle for different block sizes for the AQ2-RT model. Shaded plots indicate distances for which the model was not trained.

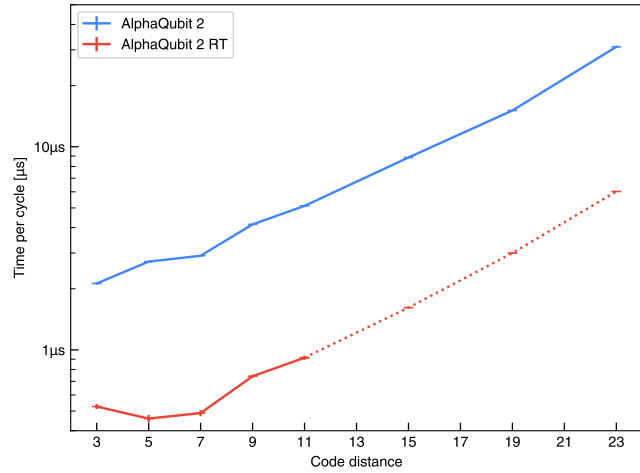


Figure S11: **Throughput of AlphaQubit 2 (AQ2).** Average time per cycle for different code distances for AQ2-full and AQ2-RT. For each model and code distance, we use the block size (24, 48 or 96) resulting in the lowest time per cycle (Fig. S10). Error bars represent 1 standard deviation. Times for AQ2-RT are shown with dotted lines at code distances for which it has not been trained.

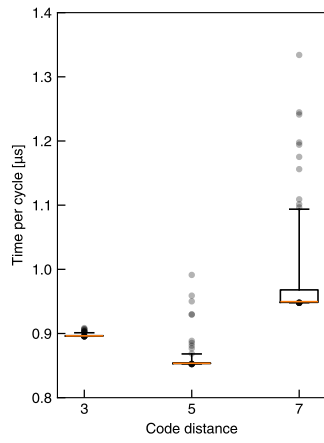


Figure S12: **Willow real-time model decoding throughput.** Box plot of throughputs for distance 3, 5 & 7 models designed for real-time operation on the Willow data, compressing blocks of 5 adjacent frames. Each boxplot represents 1000 shots of 100800 cycles processing a block of 80 frames at once. Whiskers extend from 1st to 99th percentile.  $896.6 \text{ ns} \pm 1.1$  at distance 3;  $854.3 \text{ ns} \pm 7.1$  at 5;  $965.2 \text{ ns} \pm 3.4$  at 7. Measurements are taken on a Trillium TPU.

## B.6. Latency

Since the computational cost for every block of stabilizers and of the final readout network are both fixed, the throughput and latency of the decoder are constant. While we conduct our evaluations on simulated data, and are not measuring the latency involved in the measurement and communication hardware for a real quantum computer, we can measure the latency of the decoder itself as described in [B.5](#).

We observe that the latencies in [Fig. S10b](#) do not vary with the length of the experiment, showing that the decoder can keep up with a clock rate of  $1 \mu\text{s}$ . While a small fraction of the shots show long latency, we attribute that to CPU scheduling issues that would be addressed by using a dedicated real-time operating system when running live experiments on a quantum computer.

## B.7. Achieving real-time throughput at distance 23.

AQ2 achieves higher throughputs than AQ1, due to temporal compression, parallelization across time of the spatial mixing transformer layers as well as a new hardware generation. We anticipate a number of techniques can be brought to bear to develop a faster network architecture and improve the throughput of a given architecture.

The current streaming model operates with a `bfloat16` numerical representation and we expect speed-ups by adopting 8-bit or lower precision arithmetic, which has been the focus of much recent research, and is supported in the latest and forthcoming accelerators. We have also not yet applied accelerator kernel optimizations which we expect to bring significant speed-ups. Future generations of machine learning accelerators will also bring faster computation.

The current unoptimized AQ2-full achieves a throughput of one cycle every 30 microseconds with the surface code at distance 23. Although AQ2-RT is much faster when run at distance 23 ( $6.02 \pm 0.013 \mu\text{s}$  per cycle), it is not powerful enough to achieve useful error rates. We believe that we can train an intermediate scale model from the current architecture to decode distance 23 with similar accuracy to the current full model, but significantly faster. (For instance with a careful exploration of numbers of layers, embedding sizes and increasing the number of cycles combined together).

Combining all these speed-ups may well bring us real-time decoding at distance 23 by the time that quantum computers reach this scale, but we believe that real-time decoding can be achieved by implementing a mature and optimized architecture in custom hardware (FPGA or ASIC).

## C. Baseline decoders

As explained in the main paper, we demonstrate our decoder’s accuracy by comparison with baseline decoders for the corresponding codes. For these baselines, we use a range of strong, recent decoders which are open source or to which we have access. For the surface code we are able to use the open-source decoders PyMatching and Tesseract as well as an in-house decoder Libra and the real-time matching-based decoder. These provide us with a spectrum, from the fastest, but least accurate to the slowest, but most accurate: Real-time matching decoder, PyMatching, Correlated PyMatching, Libra, Tesseract. As specified below, these decoders were run with suggested settings and on modern hardware, so we believe the timings are representative if not highly optimized.

For the colour code, we compared with Tesseract (Fig. 4b). While Chromobius[24] does support decoding the Bell-flagged colour code it does not use the flags themselves, and cannot decode the circuit that we have used. Chromobius performs better on the superdense colour code, so we use that for comparison, and note that for this code stabilizers in both bases can be read simultaneously so rounds are twice as fast as for the Bell-flagged colour code.

### C.1. PyMatching

We used PyMatching version 2.3.1 [27, 28], which solves both (uncorrelated) minimum weight perfect matching (MWPM) and correlated MWPM using the blossom algorithm. Timings were carried out on an Apple M1 Pro processor.

### C.2. Chromobius

We used Chromobius[24] version 1.1.0, also benchmarked on Apple M1 Pro processor.

### C.3. Tesseract

We use the open-source Tesseract decoder[32] (version 0.1.1, commit-sha 21fc7b0e21a028e5a25ae7cc80fd845dcb154472). This was executed on Google Cloud CPUs with 64 threads using the recommended “long-beam” configuration up to distance 11:

This configuration did not perform well with the colour code at distance 11 (needing a larger priority queue than previously needed for 120-cycle shots). Because of the computational resources required we did not evaluate beyond distance 11, and we extrapolate the accuracy

Parameter	Value
pqlimit	1,000,000
det_beam	20
beam_climbing	True
num_det_orders	21
det_order	DetIndex
no_revisit_dets	True
det_order_seed	0

Table S7: Parameters for Tesseract

based on a straight line fit of the distance 5 & 7 log logical error per cycle to indicate the logical error rates that might be achievable without speed or memory constraints.

For the surface code Tesseract and Libra performed similarly. Since Libra is much faster, we present results only for Libra.

## C.4. Libra

Libra[29] was run on a cloud-based Intel(R) Xeon(R) CPU @ 2.60GHz.

We use the “degeneracy” variant of Libra with an ensemble size of 100. The runtime of the Libra implementation we use is dominated by the computation of the complementary gap. We compute the complementary gap by modifying the detector error model to include the logical observable as a detector[57]. The resultant decoding problem breaks the assumptions required for sparse blossom to obtain almost-linear expected runtime [28]. Since the observable spans a boundary of the full 120-cycle experiment, this leads to the creation of a very large growing graph fill region. This graph fill region will grow to have very high blossom depth and saturate the  $O(n^3)$  worst-case run time within the final augmentation stage of sparse blossom (where  $n$  is the number of nodes in the DEM). This bottleneck could be removed by using a more efficient method for computing the complementary gap[58].

## D. Statistics

Throughout this article, we estimate confidence intervals in error rates using the Wilson score interval, as implemented by the statsmodels Python package v0.12.2.

## References

- [45] D Hendrycks. “Gaussian Error Linear Units (Gelus)”. In: *arXiv preprint arXiv:1606.08415* (2016).
- [46] Biao Zhang and Rico Sennrich. “Root mean square layer normalization”. In: *Advances in neural information processing systems* 32 (2019).
- [47] Jianlin Su et al. *RoFormer: Enhanced Transformer with Rotary Position Embedding*. 2023. arXiv: [2104.09864 \[cs.CL\]](https://arxiv.org/abs/2104.09864).
- [48] Geoffrey Hinton, Oriol Vinyals, and Jeff Dean. “Distilling the Knowledge in a Neural Network”. In: *arXiv:1503.02531* (2015). arXiv: [1503.02531 \[stat.ML\]](https://arxiv.org/abs/1503.02531).
- [49] Soham De et al. “Griffin: Mixing gated linear recurrences with local attention for efficient language models”. In: *arXiv [cs.LG]* (Feb. 2024).
- [50] Jacob Devlin, Ming-Wei Chang, Kenton Lee, and Kristina Toutanova. “Bert: Pre-training of deep bidirectional transformers for language understanding”. In: *Proceedings of the 2019 conference of the North American chapter of the association for computational linguistics: human language technologies, volume 1 (long and short papers)*. 2019, pp. 4171–4186.
- [51] Xiangning Chen et al. *Symbolic Discovery of Optimization Algorithms*. 2023. arXiv: [2302.06675 \[cs.LG\]](https://arxiv.org/abs/2302.06675).
- [52] K. Jordan. <https://github.com/KellerJordan/Muon>.
- [53] J Pablo Bonilla Ataides, David K Tuckett, Stephen D Bartlett, Steven T Flammia, and Benjamin J Brown. “The XZZX surface code”. In: *Nat. Commun.* 12.1 (Dec. 2021), p. 2172.
- [54] Paul Baireuther, Thomas E. O’Brien, Brian Tarasinski, and Carlo W. J. Beenakker. “Machine-learning-assisted correction of correlated qubit errors in a topological code”. In: *Quantum* 2 (Jan. 2018), p. 48. ISSN: 2521-327X. doi: [10.22331/q-2018-01-29-48](https://doi.org/10.22331/q-2018-01-29-48).
- [55] Yugo Takada and Keisuke Fujii. “Improving threshold for fault-tolerant color-code quantum computing by flagged weight optimization”. en. In: *PRX quantum* 5.3 (Sept. 2024), p. 030352.
- [56] Craig Gidney, Michael Newman, and Matt McEwen. “Benchmarking the planar honeycomb code”. en. In: *Quantum* 6.813 (Sept. 2022), p. 813.
- [57] Craig Gidney, Michael Newman, Peter Brooks, and Cody Jones. “Yoked surface codes”. In: *arXiv:2312.04522* (2023).
- [58] Nadine Meister, Christopher A. Pattison, and John Preskill. *Efficient soft-output decoders for the surface code*. 2024. arXiv: [2405.07433 \[quant-ph\]](https://arxiv.org/abs/2405.07433).